Physics-based stitching of multi-FOV PIV measurements for urban wind fields

Journal Article

Author(s):
Li, Haiwei; Zhao, Yongling (iD); Liu, Jianlin; Carmeliet, Jan

Physics-based stitching of multi-FOV PIV measurements for urban wind fields

Haiwei Li [a], Yongling Zhao [a,*], Jianlin Liu [b], Jan Carmeliet [a]

[a] *Department of Mechanical and Process Engineering, ETH Zürich, Zürich 8092, Switzerland*
[b] *College of Environmental Science and Engineering, Donghua University, Shanghai, PR China*

ABSTRACT

Particle image velocimetry (PIV) is commonly used to measure multiple field-of-views (FOVs) of the flow in large urban domains, performed in wind tunnels using an array of cameras located at fixed positions or a single camera setup that traverses during the measurements. With respect to the large amount of data produced in this type of measurement, traditional stitching approaches are no longer adequate to efficiently merge the image data. A physics-based flow field stitching method is proposed for stitching flows in urban wind fields, named regional-flow stitching. It matches the flow characteristics within neighboring FOVs of flow using a vorticity-based reference window. The method is based on finding the optimal similarity between a reference window in one FOV and another possible matching window in the other FOV. The matching window rolls in both directions at the interval of two adjacent data points, which determines the stitching resolution. The matching in flow similarity is evaluated using the normalized root-mean-squared error (*NRMSE*) between reference and possible matching windows, which is evaluated by comparison to a traditional stitching method and further verified using planar and stereo wind tunnel PIV measurement results. A comparison of computational cost with 8 FOVs and approximate 7% surface overlap between FOVs shows that our method is faster, taking about 46% of processing time, than a traditional stitching method. 3D visualization of the merged FOVs is further demonstrated with ParaView. The proposed stitching method may serve as a powerful tool for experimental studies involving large domains of urban wind flow fields.

1. Introduction

The technique of multiple field-of-view (FOV) measurements is increasingly being applied to expand the spatial domain of interest in experimental flow studies. Stitching of measurement results becomes an essential step in data-processing and advanced analyses. Wind tunnel particle image velocimetry (PIV) is a common experimental technique to investigate various topics in urban climate research [1], ranging from urban heat island (UHI) effect [2,3] to pedestrian health and comfort [4–6]. In the past, idealized generic models and single cavities were mainly studied using single camera systems [7,8]. Recent studies have started to measure large flow fields covering complex building clusters and urban areas [9,10]. However, a camera's effective coverage is sometimes limited for studies of this purpose, mainly constrained by the spatial coverage of a light sheet and the spatial resolution of the camera. A widely adopted solution to expand the spatial domain is to record particle images at a series of camera locations [4,9,11–13], which is referred to as the multi-FOV approach.

This approach has been employed in many fields of research, such as pollutants tracking [14,15], thermal image registration [16], and real-time weather monitoring [17]. In some studies, for instance, an array of multispectral and electro-optical infrared cameras is used as sensors for detecting and tracking signs of environmental contamination, where the measurement data are stitched and merged with geographic information [14,15]. Another example is the application of multi-FOV stitching to the visualization of real-time 3D weather data with high-resolution large-scale terrain [17].

In this paper, we focus on multi-FOV stitching of wind tunnel PIV images. One of the motivations is that our work may largely benefit large data processing in experimental research of flow fields around buildings and urban morphologies [3,18–20]. These studies may have large impacts on heat transfer, building energy demand [21,22], and pollutant removal [23–25]. More importantly, in most wind and water tunnel studies, the physical models are scaled-down at large ratios, typically

ranging from 1: 100 to 1: 200 [1,2,4,9,11,26–28]. Since small spatial variations in the flow field at reduced scale correspond to large changes of the actual flow at full-scale, the level of spatial resolution in these measurements depends on the accuracy of FOV stitching. From an optical point of view, sometimes multiple measurement planes have to be adopted to overcome the constraint that the laser sheet can not fully cover the domain of interest within a canopy [9]. Therefore, high-resolution fast multi-FOV stitching is nowadays essential in PIV data processing.

Current PIV experimental studies adopt different solutions to stitch measurement data. Some studies conducted synchronous measurements with a three-camera PIV system [29]. In another work [13] double frame PIV images from 12 cameras were merged into two large images prior to PIV analysis. To overcome slight misalignments and lens distortion, two large images are dewarped subsequently for image reconstruction and spaced onto a Cartesian grid with first-order polynomial mapping. The image reconstruction can also be conducted using the fast multiplicative algebraic reconstruction technique (MART) as present within LaVision 8.1 software [30]. When only a few FOVs are needed, calibration with a reference target covering the entire measurement plane can be used for stitching FOVs. This approach, however, needs specific efforts in calibration process including the project-specific target, with less flexibility in the later post-processing stage. Some of commercial softwares enable stitching for two-FOV synchronous PIV images with additional steps, which provide a simple and accurate stitching for multi-camera experimental settings. However, these stitching algorithms require more than 30% spatial overlap [31,32], where our method only needs around 12% overlap.

Due to the availability of high-speed cameras, some studies proved the practicability of using fewer cameras by conducting non-synchronous measurements separately at different locations. Moving models to expand the measurement plane is also possible when the streamwise spatial influence on wind speed and turbulence intensity is negligible [4,11]. In this type of setup, cameras are usually mounted on a high-resolution traverse system. For example, Vectoflow offers a traverse system with a resolution of 25 μm [33], and TSI offers a traverse system with a resolution of 6.25 μm [34]. The FOVs are then stitched according to the traverse system settings. When a simple arrangement of a few camera locations is implemented, roughly merging the field data can be acceptable. Moreover, in Refs. [9,35], synchronized and non-synchronized approaches are combined to maximize the spatial range of the measurement plane. The ensemble-averaged FOVs were then blended together using in-house MATLAB codes [35].

Some emerging techniques may be very helpful for stitching multi-FOVs. For example, the panorama image/video stitching used in computer vision could be adapted to process particle images or flow fields. The main procedure of general panorama stitching is the detection of distinctive key points, matching features, transformation, registration to reach a final panorama [36,37]. Compared to panorama image stitching with a central perspective projection, the projection of a PIV system is warranted to be parallel where a telecentric optics camera is usually employed guaranteeing rays passing through the camera are nearly collimated and parallel to the optical axis. Lens distortion was found to be less than 0.5 pixels [38]. The distortion, rotations, and scaling of images are negligible or can be solved in a spatial calibration process. In other words, since the images can be seen as projections on one measurement plane parallel to the cameras, the PIV FOV stitching in pre-processing only focuses on image linear overlap [39,40].

To summarize, although many studies have made attempts in stitching multi-FOVs, an accessible solution targeting high-accuracy and computationally effective stitching of PIV measurement data in wind or water tunnels is still much needed. This study proposes a method for stitching, merging and visualization of urban wind fields, using in-house Python scripts accessible in GitHub [41]. The proposed regional-flow stitching approach diagnoses flow similarity by matching flow characteristics between a vorticity-based reference window and matching windows in two neighboring FOVs. The algorithms are elaborated in section 2, and the results are discussed in section 4. In section 3, the wind tunnel experiment providing the PIV data is briefly presented. The developed method facilitates fast visualization and subsequent analyses of flow fields.

2. Methodology

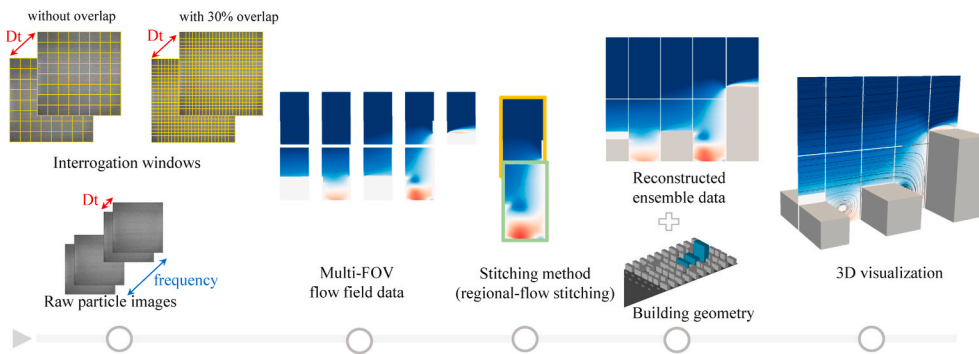### 2.1. Data-processing workflow

The proposed workflow for stitching multi-FOV PIV measurements is illustrated in Fig. 1. During a conventional calibration, each camera has to be focused on the corresponding FOV. In our method, a standard reference target can be used and moved to different camera locations to facilitate the calibration. As all the FOVs are attached to the large measurement plane, non-synchronous measurements with a single camera moving from one FOV location to another, only require a single calibration at one of the FOV locations. Comparing to traditional multi-camera calibration process using a common large target, our approach requires less effort in calibration. If cameras are individually calibrated in different grids, the two velocity fields (obtained after cross-correlation) should be mapped to have the same 'virtual' spatial resolution before performing the stitching.

In post-processing, pairs of particle images are processed using the cross-correlation algorithm available in DaVis [32] to obtain the flow field data. DynamicStudio [31] and open-source PIV postprocessing codes (e.g. MatPIV [42]) may also be used to perform cross-correlations with a selection of interrogation window size. These flow data are then time averaged, and used in the stitching method. The overlap between different FOVs is at least 5% area. The overlap between different FOVs is at least 5% area. This is not a fixed value for all experiments. Selection of the overlap region should be based on the experimental settings, providing sufficient space to filter out boundary data, and facilitating the diagnosis of flow similarity. In flows presenting a large velocity gradient, a relatively small overlap region is sufficient, while for more uniform flows, a larger overlap region is required to effectively stitch FOVs. Using a regional-flow stitching method the translation distance between FOVs is determined by finding an optimal match in flow characteristics between neighboring FOVs. The proposed regional-flow stitching method is based on matching flow similarity in the overlap areas, allowing applications to a large amount of data, which provides more flexibility in post-processing stage. Using the obtained translation distances the different FOV datasets are cropped and merged to form a new ensemble FOV dataset covering the entire measurement plane. Finally, the merged flow field data together with building models can be visualized using ParaView [38].
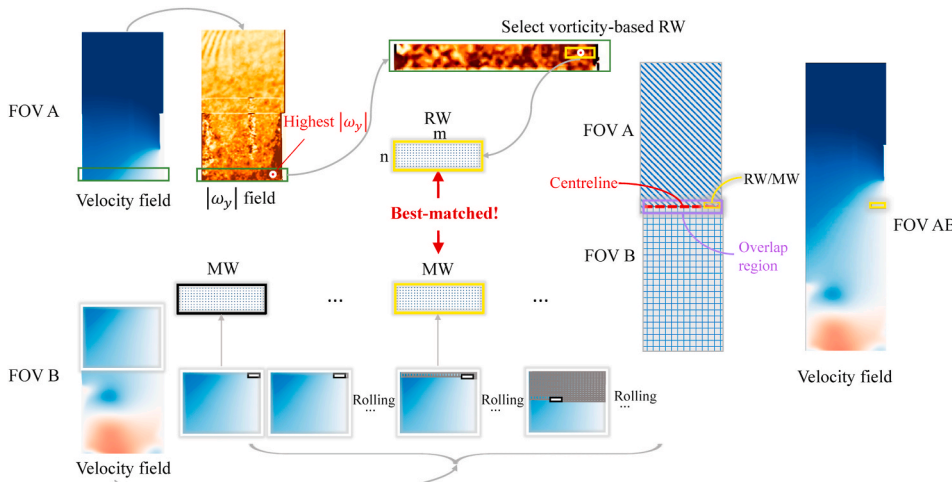
2.2. Regional-flow stitching

After proper measurement and cross-correlation processing, the velocity fields should contain the accurate result of the distribution and magnitude of velocity vectors at each timestep during a certain period. Our proposed method stitches the velocity fields. And the resolution of the stitching is the resolution of the velocity fields, which is determined by the interrogation window size and the interrogation window overlap in cross-correlation. Each FOV is linearly translated and overlap in two out of three directions. For example, for a horizontal plane, the FOVs are translated in x (streamwise) and y (spanwise) directions (refer to Fig. 3), while on a vertical plane, the FOVs should only be translated in x (streamwise) and z (height) directions.

Fig. 2 illustrates the essential steps in the proposed regional-flow stitching method. First, a reference window (RW) is selected in the FOV A, which contains n × m data points in the overlap region of FOV A with FOV B. In our test example, the two FOV have the same resolution. If the two FOV has different spatial resolutions, an additional step is required to convert all vector fields to the same spatial resolution. The

Fig. 1. Schematic diagram of data processing workflow for multi-FOV measurements. The raw particle images show a double frame measurement with Dt representing the interval between two frames and the frequency representing the number of measurements during a certain time. The yellow squares represent the interrogation windows in cross-correlation. The selection of smaller interrogation windows and larger overlap would result in the higher resolution of the velocity fields. The illustration uses the planar PIV measurements discussed in section 3. (For interpretation of the references to colour in this figure legend, the reader is referred to the Web version of this article.)

Fig. 2. Stitching process of regional-flow stitching. Two FOVs, FOV A and FOV B represent the flow field data from planar PIV measurements. The reference window (RW) and the best-matched window (MW) are marked in yellow. The black rectangles denote possible matching windows (MWs). The green rectangle denotes the overlap region. The purple rectangle denotes the overlap region after stitching and obtaining the translation distance. The centreline of RW is marked in a red dashed line. The velocity fields are represented by contour plots of the time-averaged streamwise $\overline{U}$ field. The RW and MWs contain n × m data points, where n indicates the number of rows and m indicates the number of columns. (For interpretation of the references to colour in this figure legend, the reader is referred to the Web version of this article.)
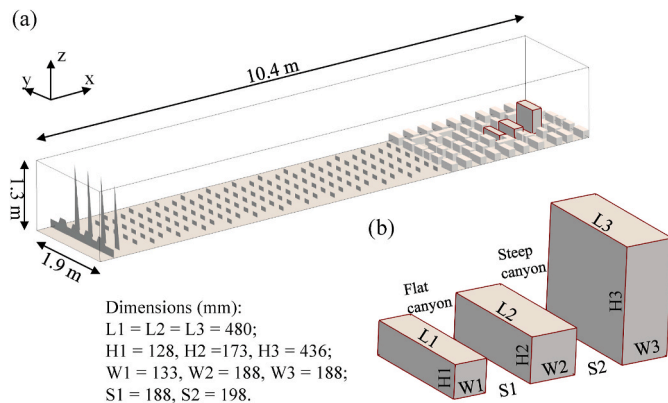
Fig. 3. (a) Wind tunnel building models and (b) Dimensions of the measurement area of interest: step-up buildings and two street canyons. The upstream canyon is noted as the flat canyon and the downstream one is noted as the steep canyon.

one with low resolution can be interpolated and mapped to a high-resolution grid. As discussed, distortions, rotations and scale effects in our images can be assumed small enough to be neglected, which means that the translation of one of the two FOVs is sufficient for stitching images. In our method, an area of n × m data points is considered to be a key region for matching. These data in the RW are referred to as reference data points.

The location of the RW is selected showing the main characteristics

of the flow field. The size of RW (data matrix n × m) should be large enough. Different sizes of RW can be selected to perform the stitching influencing the accuracy and efficiency of the method. We found that the number of reference data points should be optimally greater than 2% of the number of overlapping points. We propose to characterize the flow field by its vorticity. The out-of-plane vorticity ω_y measures the rotation at any point in the fluid by Eq. (1):

$$\omega_y = \frac{\delta \overline{W}}{\delta X} - \frac{\delta \overline{U}}{\delta Z} \qquad (1)$$

The window with the highest value of $|\omega_y|$ at its center is selected as RW (yellow rectangle in Fig. 2). Although the out-of-plane vorticity may not detect large-scale vortices, it allows detecting microscopic rotations of fluid [43]. Other flow characteristics, such as flow magnitude, could also be used to select an RW, but we found a better performance using vorticity.

In a second step, the optimal matching between this RW and all other possible matching windows (MWs) in FOV B is evaluated. Based on the experimental settings of cameras, possible matching windows are situated within the upper half of FOV B (white rectangle in Fig. 2). We note that data points at the boundaries of a FOV are neglected in the matching process because larger errors may be present there. The flow similarity between the RW and a possible MW is evaluated using the normalized root-mean-squared error (NRMSE) [44,45] of time-averaged flow components: streamwise ($\overline{U}$), spanwise ($\overline{V}$) and vertical ($\overline{W}$) velocity using Eq. (2) for planar data or Eq. (3) for stereo data:

$$NRMSE_{2D} = \left(\frac{1}{2}\right) \cdot \left(\frac{\overline{U}_{RW} - \overline{U}_{MWF}}{\overline{U}_{RWF}} + \frac{\overline{W}_{RW} - \overline{W}_{MWF}}{\overline{W}_{RWF}}\right) \times 100 \qquad (2)$$

$$NRMSE_{3D} = \left(\frac{1}{3}\right) \cdot \left(\frac{\overline{U}_{RW} - \overline{U}_{MWF}}{\overline{U}_{RWF}} + \frac{\overline{V}_{RW} - \overline{V}_{MWF}}{\overline{V}_{RWF}} + \frac{\overline{W}_{RW} - \overline{W}_{MWF}}{\overline{W}_{RWF}}\right)$$
$$\times 100$$
$$(3)$$

where $\|\cdot\|_F$ denotes the Frobenius norm, $\overline{U}_{RW}$ and $\overline{U}_{MW}$ represent the 2-dimensional streamwise velocity arrays inside the reference window and possible matching window. $\overline{W}_{RW}$ and $\overline{W}_{MW}$ represent the 2-dimensional vertical velocity arrays inside the reference window and possible matching window. $\overline{V}_{RW}$ and $\overline{V}_{MW}$ represent the 2-dimensional spanwise velocity arrays inside the reference window and possible matching window.

The location of the best-matched MW showing minimum *NRMSE* allows determining the translation distance between FOV B and FOV A (distance measured with respect to the origin). The centreline of the overlapping region can be determined by the translation distance. In the overlapping region, we keep half of the data points above/below the centreline for each FOV and merge them into a new large FOV.

The steps of the stitching process are summarized as follows:

1) Determine the location of the vorticity-based RW (marked with the yellow rectangle in Fig. 2) on the overlapping data area (marked with the green rectangle in Fig. 2) on FOV A. The center of the RW has the highest absolute value of ω_y.
2) Roll the possible MW (marked with the black rectangle in Fig. 2) having the same size of RW over the possible matching region (marked with the white rectangle in Fig. 2) with a rolling distance equal to the distance between two neighboring data points. The first MW starts from the upper right of FOV B and rolls from right to left, from top to bottom.
3) Calculate *NRMSE* between RW and MWs using Eq. (2) for planar data or Eq. (3) for stereo data.
4) The best-matched window is the MW that shows minimum *NRMSE* with the RW. The translation distances along the x-axis and z-axis can be calculated from the location of the RW and the best-matched window.
5) A centreline (the red dash line in Fig. 2) is created in the overlap region using the translation distances determined in step 4. The data of FOV A in the overlap region above the centreline and the data of FOV B in the same region below the centreline are then selected and merged with the rest of the data of FOV A and FOV B as a new ensemble FOV AB.

2.3. Coordination reconstruction and data amalgamation

With the overlap region determined, the velocity fields are trimmed along the centerline of the overlap region as discussed in step 5). A 3D coordination system by determining the global origin and the direction of the axes. And all the coordinates of the trimmed velocity fields are reconstructed according to the 3D coordination system. After that, for each timestep, velocity fields are registered and mapped according to the 3D relative positions to the origin. Finally, we obtain a reconstructed ensemble dataset in a global coordinate system. The resolution of the ensemble data remains the same as the velocity field of a single FOV. The details of this implementation can be accessed in our Python scripts in GitHub [41], including the function of trimming, repositioning and amalgamating of velocity fields.

3. Wind tunnel PIV data

The proposed stitching method is applied to PIV data measured in the ETHZ/Empa Atmospheric Boundary Layer (ABL) wind tunnel. The geometry consists of a typical urban environment at a reduced scale of 160:1 (Fig. 3). The domain of interest is the region of two step-up street canyons, shown in dark lines in Fig. 3b. Two cameras (CMOS 12 bit dual-frame cameras with the maximum spatial resolution of 2016 × 2016 pixel^2) with a Canon lens of 135 mm are used. Cameras, remote Scheimpflug, and lighting source (532 nm Nd:YAG laser of 200 mJ/pulse) are fixed on traverse arms to measure the flow fields around the area of interest. The incoming free flow velocity is 1.2 m/s that leads to Reynolds numbers of 10,240 for the flat canyon and 13,840 for the steep canyon. The PIV particle images are processed in DaVis [32]. Pairs of particle images are processed using a 2-pass cross-correlation from 64 × 64 pixels interrogation window sizes, down to 32 × 32 pixels. Fig. 4 shows the locations of FOVs reference to the three step-up buildings and the flow field data from each FOV. Nine FOVs were measured separately by planar PIV measurements on the center plane across the three step-up buildings (Fig. 4a). Each FOV consisted of two simultaneous measurements using two cameras. Nine FOVs were obtained in separate measurements by traversing the two cameras. The two synchronized cameras were positioned vertically [46], the recordings of which were stitched directly with approximately 30% spatial overlap. These neighboring FOVs are overlapping approximately 5% along the z-axis and x-axis. The four horizontal FOVs consist of stereo PIV measurements covering more than half of the area of two canyons at the roof height of the leeward building as shown in Fig. 4b. These FOVs are measured at roof level of the canyons, with FOV10 and FOV11 at 128 mm height, FOV12 and FOV13 at 173 mm height.

A statistical uncertainty analysis is carried out to determine the accuracy of the time-average flow fields. 2000 pairs of images over a period of 133 s measured at 15 Hz are used. The uncertainty is estimated with the bootstrap method [2] by selecting a number of samples out of the flow data. The coefficients of variation of *U* and *TKE* are calculated using Eq. (4):

$$c_{V,\,U} = \frac{\sigma(U_n)}{\overline{U}_n} \;,\; c_{V,TKE} = \frac{\sigma(TKE_n)}{\overline{TKE}_n} \;. \qquad (4)$$

We select for the uncertainty analysis the data for the middle region of FOV3 (see Fig. 4a). The coefficients of variation agree with the result reported in Tsalicoglou et al. [2], following an exponential decay with an increasing number of samples. As the number of samples reaches 1500, the coefficient of variation for the TKE reaches 2.20% and the coefficient of variation for U reaches 0.66%, which is considered to guarantee sufficient accuracy. After n = 1500, the coefficient of variation for U maintains a very low value with little deviation from 0.66%. The uncertainty analysis proves an accurate mean flow when averaging more than 1500 instant flow fields at 15 Hz measurement frequency.

4. Results and discussion

In this section, the regional-flow stitching is applied to planar and stereo wind tunnel PIV measurements. For verification purposes, our stitching results are compared to the results obtained from a reference stitching method using stitching along a line as described in appendix A.

4.1. Stitching vertical planar-measurements

The proposed regional-flow stitching is firstly applied to the planar data ($\overline{U}$ and $\overline{W}$) of the neighboring FOV2 and FOV6 (refer to Fig. 4a). The FOV area is 376.4229 mm × 208.1246 mm, and the overlap region is approximately 7% of the total area containing more than 1300 data points. Fig. 5a shows the mean flow after regional-flow stitching of the two FOVs, where the $NRMSE_{2D}$ of the reference data points and the best-
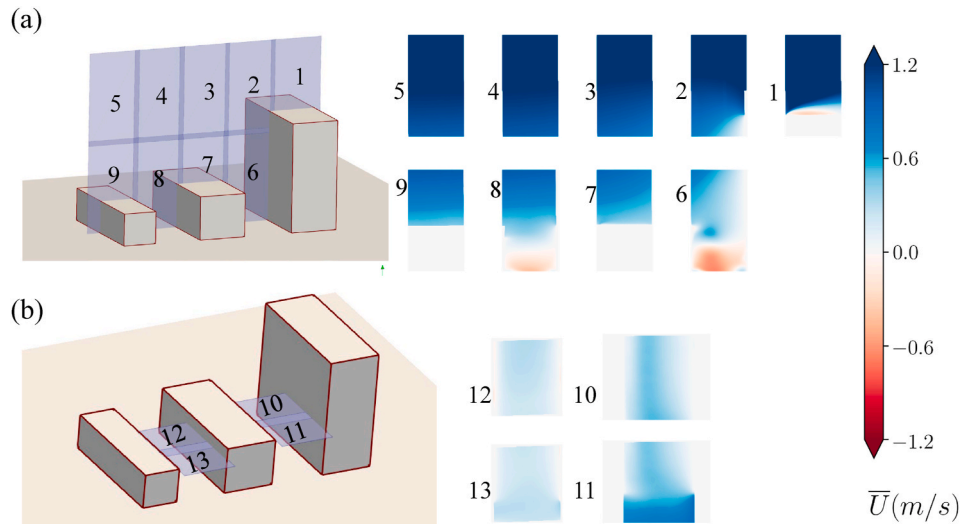
Fig. 4. FOV locations (in light purple) on the PIV measurement planes, with (a) showing FOV1~9 covering the center vertical plane across the buildings, and (b) showing FOV10 and FOV11 on 173 mm and FOV12 and FOV13 on 128 mm above the ground. The flow fields in FOVs are shown using the contour plots of $\overline{U}$ fields. (For interpretation of the references to colour in this figure legend, the reader is referred to the Web version of this article.)
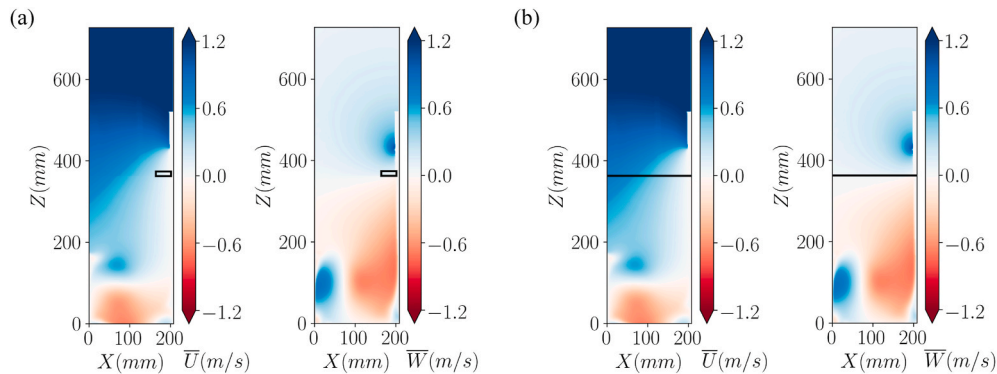
Fig. 5. Contour plots of $\overline{U}$ and $\overline{W}$ on the merged FOV2 and FOV6 plane. (a) Stitched results using the regional-flow stitching method with the reference window marked in black, and (b) stitched results using the reference method with the stitched line marked in black.

matched data points is 3.87%. Fig. 5b shows the stitched results using the reference stitching method (refer to Appendix A). The translation distance is determined to be 350.7286 mm using the region-flow stitching, which is the same obtained from the reference stitching method and close to the recorded value from the traverse system (350 mm with an accuracy of 1 mm). This shows that both regional-flow and linear-flow stitching give similar results and can be applied to merge PIV data.

Our method is designed for experiments measuring the atmospheric turbulent flow. In the urban canopy layer (UCL) and roughness sub-layer (RSL), turbulence mainly depends on spatial characteristics [47]. In the inertial sub-layer (ISL), turbulent fluxes can be mostly constant with height, where the logarithmic wind laws can be applied [48,49]. In our experiment, the overlap region is around 7%, covering Z = 350–361.71 mm. It is worth noting that this overlap ratio is not very important so long as the overlap is in the flow having a prominent velocity gradient. Comparing to flows in UCL, the velocity gradient is less dependent on the urban morphology. The generated flow follows the logarithmic wind laws in the overlap region. The *NRMSE* successfully characterizes the velocity gradient and detects the best-matched window. For extreme cases with uniform flow, velocity gradient might be not sufficient to characterize the flow. If other variables have conspicuous variations and dominant characteristics, improvements of Eq. (2) and Eq. (3) are expected.

4.2. Stitching horizontal stereo-measurements

Stitching is also applied on the horizontal stereo-measurements ($\overline{U}$, $\overline{V}$ and $\overline{W}$) in neighboring FOVs 10–11 and 12–13. Fig. 6 shows the contour plots of stream-, span- and vertical time-averaged velocity in the two street canyons for the regional-flow stitching method. On the horizontal measurement plane, the FOVs are translated towards the y-axis direction. The reference window contains 10 × 30 data points, with is roughly 2.77% of the number of overlapping points, higher than the value of 2% mentioned in section 2.2. The best-matched result is obtained with a *NRMSE* of 4.80%. The white lines separate different FOVs. The results show smooth transitions of the velocity components ($\overline{U}$, $\overline{V}$ and $\overline{W}$) among neighboring FOVs.

4.3. Use of time-averaged flow field data

In our proposed stitching method, we use time-averaged flow field data ensuring adequate accuracy and resolution. The first reason to use time-averaged flow field data for stitching is to eliminate errors appearing in time-dependent PIV measurement. Non-uniform laser intensity profile and surface reflections may lead to local erroneous light intrusion in particle images [50,51]. Time-averaging allows to largely eliminate these local errors appearing in the PIV images. Secondly, we note that time-averaged flow still reflects the main characteristics of
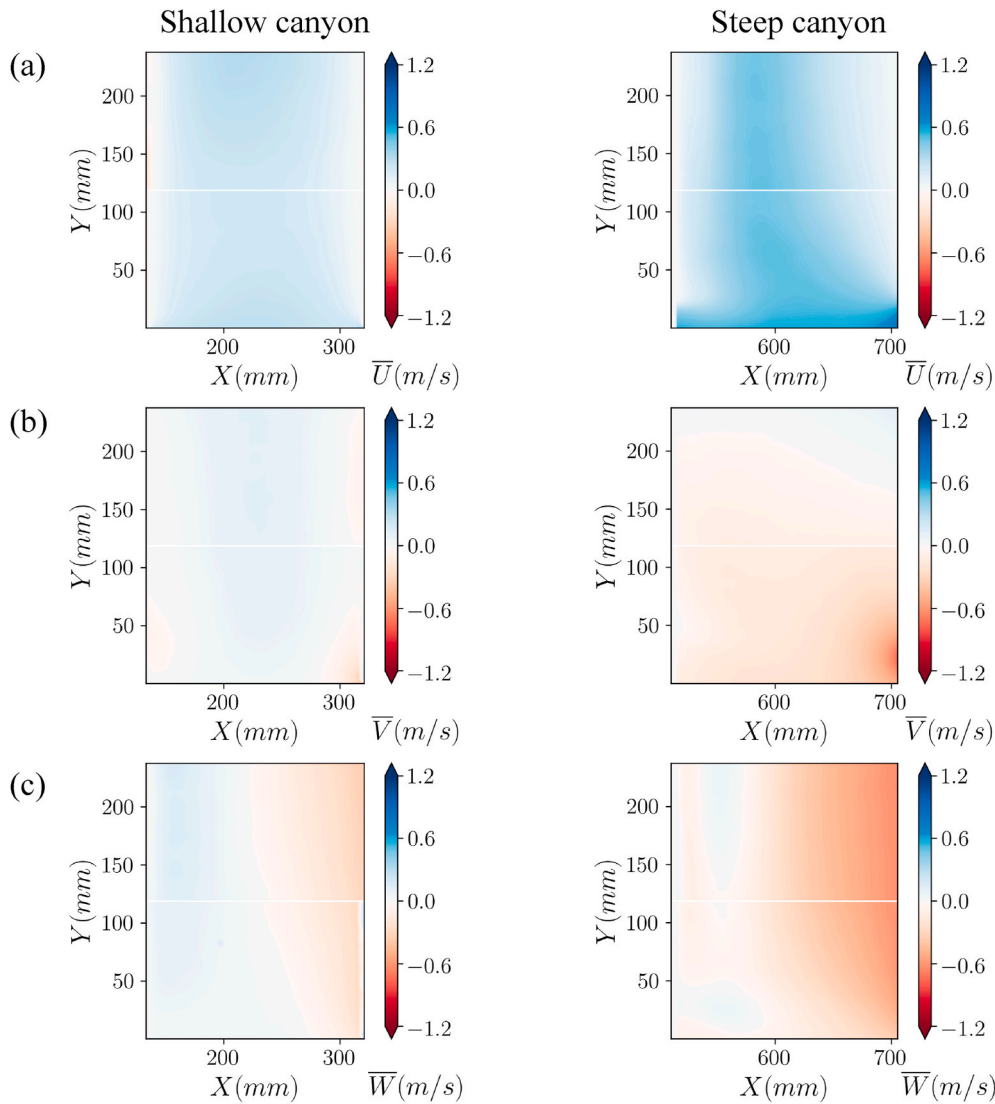
Fig. 6. Contour plots of the merged data in the horizontal measurement plane on the roof level, with (a) showing $\overline{U}$, (b) showing $\overline{V}$ and (c) showing $\overline{W}$. On each subplot, the left plot represents the results for the upstream flat canyon and the right plot represents the results for the downstream steep canyon.

urban flows, such as a logarithmic wind law, shear layers and recirculation zones in urban structures [52]. This type of time-averaged flow matching was also proved to be effective in the literature [35], where ensemble-averaged FOVs were stitched.

The uncertainty analysis shows that an adequate number of samples is necessary for averaging. The resolution of our stitching method depends on the interval between two neighboring data points or between two neighboring matching windows (the possible matching window moves at this interval to find the best-matched window). A smaller interrogation window containing fewer pixels or using high overlap (e.g. 75%) in particle images cross-correlation processing could effectively help achieve higher resolution in stitching.

4.4. Location and size of reference window in two-dimensional stitching

Compared to the reference method (at-line-flow stitching), which considers the velocity similarity in only one dimension (1D), our 2D stitching method evaluates the flow similarity of the velocity profiles in both directions. In the ISL, normally 2–5H above the ground, the turbulence is homogeneous and fluxes vary very little with height [53–55]. In contrast, in the urban canopy layer, within 1H (reference building height) from the ground, the flow and turbulence are spatially varying a

lot (e.g. in shear layers). Vorticity is recommended to be used as a flow indicator when velocity gradients over the stitching region are not too large. The out-of-plane vorticity detects the microscopic rotations at any location of fluid [43]. It can sufficiently detect the vortex structures of the turbulent fluids. For the upper part of ISL, where the flows receive little influence from building models, the flows have little variance in streamwise, and following the logarithm law in the vertical direction. Therefore, only vertical stitching is necessary. And we could select the RW with other flow indicators, for instance, velocity gradient in the vertical direction. In our application of the stitching method, the overlap regions are sufficiently above the urban canopy layer and near the ISL, at around 2.7H above the ground.

We showed above that we can effectively stitch the flow fields using a 2D reference window with a size of 10 × 30 reference data points. In section 2.2, it was mentioned that more than 2% of overlapping data points are expected to be used as reference data points. We also mention that a larger reference window will lead to faster computation. However, the size of the reference window is restricted, so the RW remains inside the overlap region. Fig. 7 shows the *NRMSE* versus iterations for MWs moving in space, with a size of 10 × 30 and 10 × 60 reference data points, respectively. As the moving MW approaches the best matching with the reference window, the *NRMSE* follows a decreasing trend until
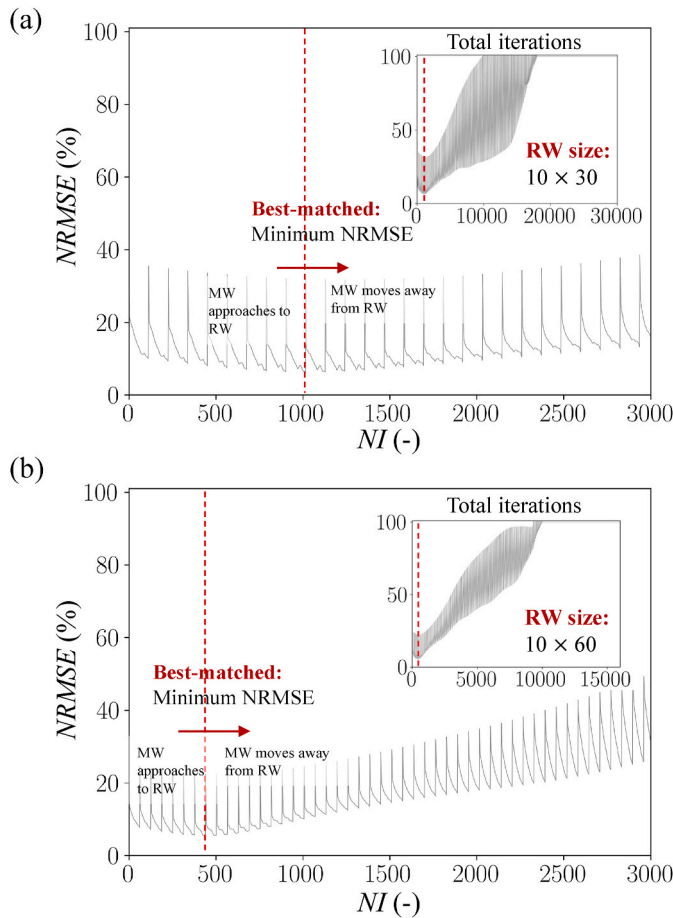
Fig. 7. *NRMSE* versus the number of iteration (*NI*) during the stitching of FOV2 and FOV6 using the regional-flow stitching method. The minimum *NRMSE* happens with the best-matched windows. (a) Represents the result for stitching with 10 × 30 reference data points and (b) represents the result for stitching with 10 × 60 reference data points. RW represents the reference window and MW represents the possible matching window. The upper right graphs show the variation of the *NRMSE* during the whole matching process.

the best-matched window is found. When the MW moves away from the best matching with the reference window and mismatching increases, the *NRMSE* gradually increases. It is clear that for the large RW (Fig. 7b) fewer iterations are needed, which significantly reduces the needed computational power. The size of RW should be large enough to better capture the flow characteristics. Larger RW can also save computational costs. In practice, it is preferable to select a larger reference window containing more reference data points, as long as the reference window is limited within the overlap area.

4.5. Evaluation of the stitching performances

The processing efficiency and effectiveness of the stitching method are evaluated in this section. The test is carried out using a workstation with 8 cores, 16 processors (Intel(R) Core(TM) i9-9880H CPU @ 2.30 GHz). From Table 1, the processing time of regional-flow stitching is less than 46% of the processing time of the reference method. The reason is

Table 1
Comparison of the processing time.

	2 FOVs	4 FOVs	8 FOVs
Regional-flow stitching (t)	2.59 s	4.56 s	9.23 s
Reference method (t*)	5.89 s	10.33 s	20.43 s
t/t*	43.97%	44.14%	45.18%

that the selection of the size of the reference window allows matching more reference data points at once, instead of matching some discrete data points at a line. Fewer iterations are required in the regional-flow stitching, therefore, results in less time. In terms of effectiveness, the proposed method achieves a resolution of 1.2848 mm which is the spatial interval of neighboring data points in both directions determined by the size and overlapping ratio of interrogation windows. The spatial resolution can be further improved by increasing data points in FOVs directly (using a smaller interrogation window) or indirectly (using a higher overlapping ratio in cross-correlation) in particle images cross-correlations. A higher overlapping ratio results in more interrogation windows and hence more data points for a given FOV, allowing the MW to traverse at a greater spatial resolution.

4.6. Coordination reconstruction and visualization

The reconstructed ensemble dataset is stored in a format readable in ParaView [56] with 3D dimensional information. We mention that importing an ensemble flow field is much faster than importing FOVs separately. This means that postprocessing computations and analysis are much faster and easier with our stitched data in ParaView. Together with the building models, the measurement data can be visualized in 3D. An example of the visualization is shown in Fig. 8. The horizontal planes and the vertical plane are integrated with the geometry of building models. The flow structures and the interactions with building geometries can be clearly observed in any perspective view, which gives a comprehensive view of the large-scale flow around the urban area. The flows are well-presented at a high level of spatial resolution. More detailed observations and analyses are possible for the local flows around the building structures.

5. Conclusions

This work proposes an effective solution to the multi-FOV PIV (multiple field-of-view, particle image velocimetry) data stitching and processing. A workflow is summarized, from the raw particle image data to an ensemble reconstructed dataset for subsequent data analysis and visualization in ParaView. A fast physics-based stitching algorithm is developed and implemented in Python and verified using wind tunnel measurement data. The algorithm is designed to stitch turbulent flows in atmospheric conditions. The tests are performed in the UCL and lower ISL, the results of which prove that the method can detect the flow similarity in different FOVs measuring an urban wind field.

Our stitching method, regional-flow stitching, can diagnose and analyze the flow characteristics to identify the flow similarity in multiple FOVs. It detects the best-matched points between neighboring field-of-views of flow within a vorticity-based 2D reference window. The spatial resolution of the proposed stitching method is at the level of the distance between two neighboring data points. The wind tunnel PIV data
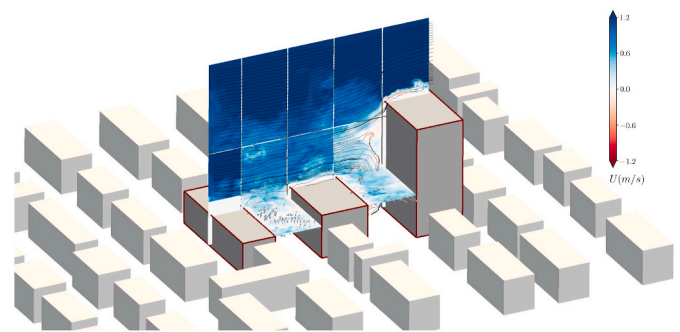
Fig. 8. One example of visualization of reconstructed *U* of the vertical and horizontal flow fields at one single timestep. The ensembled field includes 13 FOVs in total.

from both planar and stereo measurements are used for the verification of thirteen FOVs. The stitching performance may be further improved by matching other flow characteristics and using an optimized reference window size.

Our method contributes to fast data processing of wind or water tunnel PIV measurements of urban wind fields involving multi-FOVs. Comparing to the current practices, the proposed method requires less effort in spatial calibration, less spatial overlap and is applicable to both synchronous and non-synchronous PIV measurements. Moreover, the method is a data-driven method, which provides more flexibility in post-processing. The 3D visualization of a new ensemble flow field with the building models facilities detailed analyses of large-scale urban flows. The stitching and visualization methods encourage the application of multi-FOV measurements to expand the domain of interest in experimental studies with the increased use of cameras and recording locations. The expanded spatial coverage and high resolution in PIV measurements potentially enable more possibilities in optimizing urban

scale microclimate designs.

Appendix A. Reference method: at-line-flow stitching

The at-line-flow stitching method is a straightforward solution to stitch flow fields, which is used as a reference method in section 4. The main idea of this stitching method is to select a reference line (RL) in the overlap region on one of the FOV (FOV A). And we find another line in the other FOV (FOV B) that matches the velocity profile with the reference one (Fig. A.1). This method is inspired by the characteristics of 1D spatial variations of the time-averaged streamwise velocity $\overline{U}$ and time-averaged vertical velocity $\overline{W}$. After we find the best-matched line, the translation distance is therefore determined. Since the velocity in the incoming flow direction ($\overline{U}$) as the dominant parameter, the data matching and comparison are conducted with the $\overline{U}$ field. In practice, if other variables have conspicuous variations and dominant characteristics along the axes, the $\overline{U}$ might be replaced. The matching process also allows certain tolerance (σ), which should be set according to the actual measurement setup, normally below 5%. The stitching process could be summarized in the following steps, assuming that the FOV A and FOV B are overlapping along the z-axis.
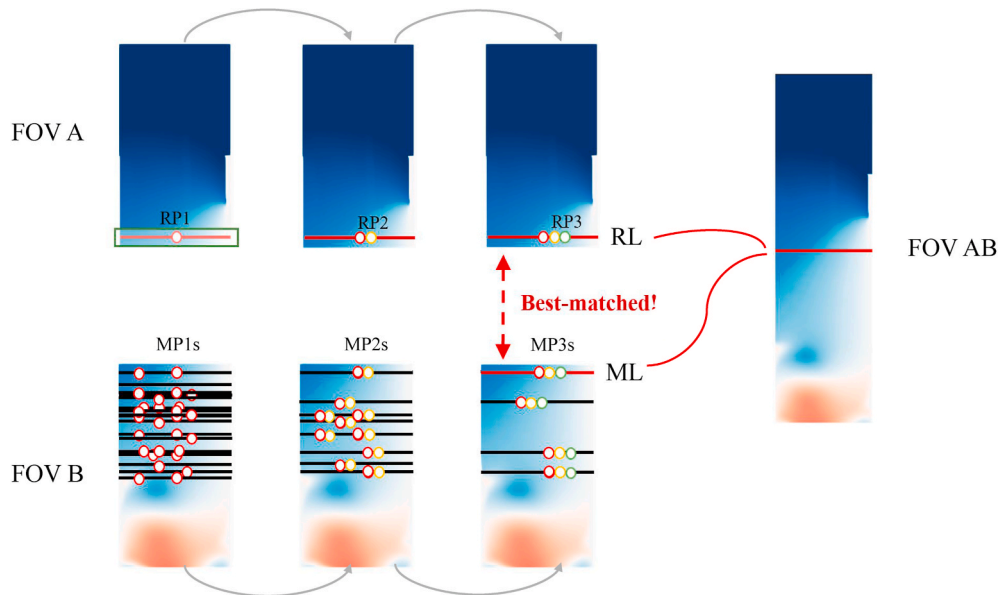
Fig. A.1. Stitching process of the reference method. The demonstration uses the flow field data from planar PIV measurements. RP denotes reference point and MP denotes matched points. RL represents the reference line and ML represents the possible matching line.

1) Select the RL in roughly the middle of the overlap region of FOV A, which is to ensure our reference line being within the overlapping area. And then, select the center data point of the line as the first reference point (RP1).
2) Match the first reference point (RP1) with all the points in the FOV B. With a certain tolerance (σ), we may obtain several matched points (MP1s) that match with the reference point (RP1), by Eq A.1.

$$\left| \overline{U}_{RP1} - \overline{U}_{MP1} \right| < = \sigma \cdot \overline{U}_{RP1} \tag{A.1}$$

where $\overline{U}_{RP1}$ denotes the streamwise velocity of the RP1 and $\overline{W}_{RP1}$ denotes the streamwise velocity of the MP1. σ represents the matching tolerance.

3) Select the point (RP2) on the right of the first reference point as the second reference point. Match the RP2 with the points on the right of the first matched points, by Eq A.2. Fewer matched points (MP2s) are matched this time.

$$\left| \overline{U}_{RP2} - \overline{U}_{MP2} \right| < = \ \sigma \cdot \overline{U}_{RP2} \tag{A.2}$$

4) Iterate step 3) with the third reference point (RP3) on the right of the matched points. Continue the iterations until the minimum possible matching lines (MLs) are left.
5) The *NRMSE* of RL and MLs is estimated using Eq A.3, according to the literature [44,45].

$$NRMSE = \left(\frac{1}{2}\right) \cdot \left(\frac{\left\| \overline{U}_{RL} - \overline{U}_{ML} \right\|_F}{\left\| \overline{U}_{RL} \right\|_F} + \frac{\left\| \overline{W}_{RL} - \overline{W}_{ML} \right\|_F}{\left\| \overline{W}_{RL} \right\|_F} \right) \times 100 \tag{A.3}$$

where $\overline{U}_{RL}$ and $\overline{U}_{ML}$ denotes the streamwise velocity arrays of the points on RL and ML, and $\overline{W}_{RL}$ and $\overline{W}_{ML}$ denotes the vertical (height) direction velocity arrays of the points on RL and ML.

6) Select the one with the minimum *NRMSE* as the best-matched line. And calculate the translation distances according to the coordination of the reference line and matched line.
7) Conduct the same matching process to the points to the left to check the accuracy and other possibilities. Stitch the best-matched line with the reference line.

Appendix B. Data and script management

Python scripts for the proposed stitching method along with the data reconstruction scripts are publicly available in GitHub [41]. The measurement data used for method verification are available upon request.

References

[1] Y. Zhao, L.W. Chew, A. Kubilay, J. Carmeliet, Isothermal and non-isothermal flow in street canyons: a review from theoretical, experimental and numerical perspectives, Build. Environ. 184 (2020), 107163, https://doi.org/10.1016/j.buildenv.2020.107163.

[2] C. Tsalicoglou, J. Allegrini, J. Carmeliet, Non-isothermal flow between heated building models, J. Wind Eng. Ind. Aerod. 204 (2020), 104248, https://doi.org/10.1016/j.jweia.2020.104248.

[3] J. Allegrini, A wind tunnel study on three-dimensional buoyant flows in street canyons with different roof shapes and building lengths, Build. Environ. 143 (2018) 71–88, https://doi.org/10.1016/j.buildenv.2018.06.056.

[4] L. Manickathan, T. Defraeye, J. Allegrini, D. Derome, J. Carmeliet, Comparative study of flow field and drag coefficient of model and small natural trees in a wind tunnel, Urban For. Urban Green. 35 (2018) 230–239, https://doi.org/10.1016/j.ufug.2018.09.011.

[5] J. Hang, Y. Li, M. Sandberg, R. Buccolieri, S. Di Sabatino, The influence of building height variability on pollutant dispersion and pedestrian ventilation in idealized high-rise urban areas, Build. Environ. 56 (2012) 346–360, https://doi.org/10.1016/j.buildenv.2012.03.023.

[6] D. Cui, G. Hu, Z. Ai, Y. Du, C.M. Mak, K. Kwok, Particle image velocimetry measurement and CFD simulation of pedestrian level wind environment around U-type street canyon, Build. Environ. 154 (2019) 239–251, https://doi.org/10.1016/j.buildenv.2019.03.025.

[7] G.T. Johnson, L.J. Hunter, Urban wind flows: wind tunnel and numerical simulations - a preliminary comparison, Environ. Model. Software 13 (3–4) (1998) 279–286, https://doi.org/10.1016/S1364-8152(98)00028-0.

[8] H. Takimoto, A. Sato, J.F. Barlow, R. Moriwaki, A. Inagaki, S. Onomura, M. Kanda, Particle image velocimetry measurements of turbulent flow within outdoor and indoor urban Scale Models and flushing Motions in urban canopy Layers, Boundary-Layer Meteorol. 140 (2011) 295–314, https://doi.org/10.1007/s10546-011-9612-6.

[9] M.A. Ferreira, B. Ganapathisubramani, PIV-based pressure estimation in the canopy of urban-like roughness, Exp. Fluid 61 (2020), 70, https://doi.org/10.1007/s00348-020-2904-1.

[10] Y. Zhao, H. Li, A. Kubilay, J. Carmeliet, Buoyancy effects on the flows around flat and steep street canyons in simplified urban settings subject to a neutral approaching boundary layer: wind tunnel PIV measurements, Sci. Total Environ. 797 (2021), 149067, https://doi.org/10.1016/J.SCITOTENV.2021.149067.

[11] J. Allegrini, B. Lopez, The influence of angular configuration of two buildings on the local wind climate, J. Wind Eng. Ind. Aerod. 156 (2016) 50–61, https://doi.org/10.1016/j.jweia.2016.07.008.

[12] C. Vanderwel, B. Ganapathisubramani, Turbulent boundary layers over multiscale rough patches, Boundary-Layer Meteorol. 172 (2019) 1–16, https://doi.org/10.1007/s10546-019-00430-x.

[13] C.F.V. Carmer, A. Heider, A. Schröder, R. Konrath, J. Agocs, A. Gilliot, J.C. Monnier, Evaluation of large-scale wing vortex wakes from multi-camera PIV measurements in free-flight laboratory, Top. Appl. Phys. 112 (2007) 377–394, https://doi.org/10.1007/978-3-540-73528-1_20.

[14] M. Lega, J. Kosmatka, C. Ferrara, F. Russo, R.M.A. Napoli, G. Persechino, Using advanced aerial platforms and infrared thermography to track environmental contamination, Environ. Forensics 13 (4) (2012) 332–338, https://doi.org/10.1080/15275922.2012.729002.

[15] M. Lega, G. Persechino, GIS and infrared aerial view: advanced tools for the early detection of environmental violations, WIT Trans. Ecol. Environ. 180 (2014) 225–235, https://doi.org/10.2495/WM140191.

[16] A. Irani Rahaghi, U. Lemmin, D. Sage, D.A. Barry, Achieving high-resolution thermal imagery in low-contrast lake surface waters by aerial remote sensing and image registration, Remote Sens. Environ. 221 (2019) 773–783, https://doi.org/10.1016/j.rse.2018.12.018.

[17] C.D. Shaw, F.T.Y. Jiang, R.M. Parry, B. Plale, A.A. Wasilewski, W. Ribarsky, N.L. Faust, Real-time weather data on terrain, in: Vis. Temporal Spat. Data Civ. Def. Appl., International Society for Optics and Photonics, 2001, pp. 1–8.

[18] R.A. Memon, D.Y.C. Leung, C.H. Liu, Effects of building aspect ratio and wind speed on air temperatures in urban-like street canyons, Build. Environ. 45 (1) (2010) 176–188, https://doi.org/10.1016/j.buildenv.2009.05.015.

[19] Y. Fan, Q. Wang, S. Yin, Y. Li, Effect of city shape on urban wind patterns and convective heat transfer in calm and stable background conditions, Build. Environ. 162 (2019), 106288, https://doi.org/10.1016/j.buildenv.2019.106288.

[20] Y. Du, C.M. Mak, J. Liu, Q. Xia, J. Niu, K.C.S. Kwok, Effects of lift-up design on pedestrian level wind comfort in different building configurations under three wind directions, Build. Environ. 117 (2017) 84–99, https://doi.org/10.1016/j.buildenv.2017.03.001.

[21] J. Allegrini, V. Dorer, J. Carmeliet, Influence of the urban microclimate in street canyons on the energy demand for space cooling and heating of buildings, Energy Build. 55 (2012) 823–832, https://doi.org/10.1016/j.enbuild.2012.10.013.

[22] O.A. Pol, D. Robinson, Impact of urban morphology on building energy needs: a review on knowledge gained from modeling and monitoring activities, in: Proc. CISBAT 2011 - CleanTech Sustain. Build., 2011, pp. 943–948.

[23] H. Huang, Y. Akutsu, M. Arai, M. Tamura, A two-dimensional air quality model in an urban street canyon: evaluation and sensitivity analysis, Atmos. Environ. 34 (5) (2000) 689–698, https://doi.org/10.1016/S1352-2310(99)00333-7.

[24] J.J. Baik, J.J. Kim, A numerical study of flow and pollutant dispersion characteristics in urban street canyons, J. Appl. Meteorol. 38 (11) (1999) 1576–1589, https://doi.org/10.1175/1520-0450(1999)038<1576:ANSOFA>2.0.CO;2.

[25] P. Edussuriya, A. Chan, A. Ye, Urban morphology and air quality in dense residential environments in Hong Kong. Part I: district-level analysis, Atmos. Environ. 45 (27) (2011) 4789–4803, https://doi.org/10.1016/j.atmosenv.2009.07.061.

[26] S. Karra, L. Malki-Epshtein, M.K.A. Neophytou, Air flow and pollution in a real, heterogeneous urban street canyon: a field and laboratory study, Atmos. Environ. 165 (2017) 370–384, https://doi.org/10.1016/j.atmosenv.2017.06.035.

[27] J. Allegrini, V. Dorer, J. Carmeliet, Wind tunnel measurements of buoyant flows in street canyons, Build. Environ. 59 (2013) 315–326, https://doi.org/10.1016/j.buildenv.2012.08.029.

[28] Y. Fan, Y. Li, Q. Wang, S. Yin, TIV and PIV based natural convection study over a square flat plate under stable stratification, Int. J. Heat Mass Tran. 140 (2019) 660–670, https://doi.org/10.1016/j.ijheatmasstransfer.2019.06.031.

[29] J.I. Cardesa, T.B. Nickels, J.R. Dawson, 2D PIV measurements in the near field of grid turbulence using stitched fields from multiple cameras, Exp. Fluid 52 (2012) 1611–1627, https://doi.org/10.1007/s00348-012-1278-4.

[30] K.P. Lynch, F. Scarano, Experimental determination of tomographic PIV accuracy by a 12-camera system, Meas. Sci. Technol. 25 (8) (2014), 084003, https://doi.org/10.1088/0957-0233/25/8/084003.

[31] DynamicStudio, (2021). https://www.dantecdynamics.com/components/dynamicstudio/(accessed July 15, 2021).

[32] DaVis 10, (2021). https://www.lavision.de/en/products/davis-software/(accessed July 15, 2021).

[33] Vectoflow, (2021). https://www.vectoflow.de/en/products/traversing-system/(accessed July 15, 2021).

[34] TSI Traverse System, (2021). https://tsi.com/product-accessories/traverse-systems-t2d/(accessed July 15, 2021).

[35] C. Kumar, P. Manovski, M. Giacobello, Particle Image Velocimetry measurements on a generic submarine hull form, in: Proc. 18th Australas. Fluid Mech. Conf. AFMC 2012, 2012.

[36] S. Pravenaa, R. Menaka, A methodical review on image stitching and video stitching techniques, Int. J. Appl. Eng. Res. 11 (5) (2016) 3442–3448.

[37] K. Chen, M. Wang, Image stitching algorithm research based on OpenCV, in: Proc. 33rd Chinese Control Conf. CCC 2014, 2014, https://doi.org/10.1109/ChiCC.2014.6896208.

[38] H.-G. Maas, Photogrammetric techniques in multi-camera tomographic PIV, in: Proc. 8th Int. Symp. Par-Ticle Imaging Velocim, 2009.

[39] Y. Zhu, M. Sun, X. Chen, H. Li, Q. Mu, D. Li, L. Xuan, Single full-FOV reconstruction Fourier ptychographic microscopy, Biomed. Opt Express 11 (12) (2020) 7175–7182, https://doi.org/10.1364/boe.409952.

[40] X. Chen, W. Zhou, X. Cai, M. Su, H. Liu, In-line imaging measurements of particle size, velocity and concentration in a particulate two-phase flow, Particuology 13 (2014) 106–113, https://doi.org/10.1016/j.partic.2013.03.005.

[41] H. Li, Scripts: MultiFOV-PIV-Data-Stitching, 2021. https://github.com/florahww/MultiFOV-PIV-Data-Stitching.git.

[42] MatPIV, (2021). https://www.mn.uio.no/math/english/people/aca/jks/matpiv/.

[43] J.C.R. Hunt, a a Wray, P. Moin, Eddies, streams, and convergence zones in turbulent flows, Cent. Turbul. Res. Proc. Summer Progr. (1988) 193–208.

[44] H.P. Wang, Q. Gao, S.Z. Wang, Y.H. Li, Z.Y. Wang, J.J. Wang, Error reduction for time-resolved PIV data based on Navier–Stokes equations, Exp. Fluid 59 (2018), 149, https://doi.org/10.1007/s00348-018-2605-1.

[45] D. Garcia, A fast all-in-one method for automated post-processing of PIV data, Exp. Fluid 50 (2011) 1247–1259, https://doi.org/10.1007/s00348-010-0985-y.

[46] Y. Zhao, C. Lei, J.C. Patterson, PIV measurements of the K-type transition in natural convection boundary layers, Exp. Therm. Fluid Sci. 101 (2019) 62–75, https://doi.org/10.1016/j.expthermflusci.2018.09.007.

[47] M.W. Rotach, On the influence of the urban roughness sublayer on turbulence and dispersion, in: Atmos. Environ., 1999, https://doi.org/10.1016/S1352-2310(99)00141-7.

[48] H. Tennekes, The logarithmic wind profile, J. Atmos. Sci. 30 (2) (1973) 234–238, https://doi.org/10.1175/1520-0469(1973)030<0234:tlwp>2.0.co;2.

[49] M. Núñez Peiró, C. Sánchez-Guevara Sánchez, F.J. Neila González, Source area definition for local climate zones studies. A systematic review, Build. Environ. 148 (2019) 258–285, https://doi.org/10.1016/j.buildenv.2018.10.050.

[50] J. Nogueira, A. Lecuona, P.A. Rodriguez, Local field correction PIV: on the increase of accuracy of digital PIV systems, Exp. Fluid 27 (1999) 107–116, https://doi.org/10.1007/s003480050335.

[51] E. Limacher, C. Morton, D. Wood, On the calculation of force from PIV data using the generalized added-mass and circulatory force decomposition, Exp. Fluid 60 (2019), 4, https://doi.org/10.1007/s00348-018-2648-3.

[52] P. Kastner-Klein, M.W. Rotach, Mean flow and turbulence characteristics in an urban roughness sublayer, Boundary-Layer Meteorol. 111 (2004) 55–84, https://doi.org/10.1023/B:BOUN.0000010994.32240.b1.

[53] J.F. Barlow, Progress in observing and modelling the urban boundary layer, Urban Clim 10 (2014) 216–240, https://doi.org/10.1016/j.uclim.2014.03.011.

[54] J. Zou, Y. Yu, J. Liu, J. Niu, K. Chauhan, C. Lei, Field measurement of the urban pedestrian level wind turbulence, Build. Environ. 194 (2021), 107713.

[55] J. Liu, X. Zhang, J. Niu, K.T. Tse, Pedestrian-level wind and gust around buildings with a 'lift-up' design: assessment of influence from surrounding buildings by adopting LES, Build. Simul. 12 (2019) 1107–1118, https://doi.org/10.1007/s12273-019-0541-5.

[56] ParaView-5.9.0, (2021). https://www.paraview.org/.